

# Electronic regulation of Ni single atom by confined Ni nanoparticles for energy-efficient CO<sub>2</sub> electroreduction

Wenhao Ren,<sup>†</sup> Xin Tan,<sup>†</sup> Chen Jia, Anna Krammer, Qian Sun, Jiangtao Qu, Sean C. Smith, Andreas Schueler, Xile Hu\* and Chuan Zhao\*

**Abstract:** The electronic modulation of single-atom catalysts represents a fundamental way to achieve superior performance. However, the modification of atomically dispersed active sites remains a huge challenge. Here we show a cooperative Ni single-atom on nanoparticle catalyst (NiSA/NP) via direct solid-state pyrolysis, where Ni nanoparticles donate electrons to Ni(i)-N-C sites via carbon nanotubes network, achieves a high CO current density of 352 mA cm<sup>-2</sup> at -0.55 V vs RHE in an alkaline flow cell. When coupled with a NiFe-based oxygen evolution anode into a zero-gap membrane electrolyser, it delivers an industrial-relevant CO current density of 310 mA cm<sup>-2</sup> at a low cell voltage of -2.3 V, corresponding to an overall energy efficiency of 57%. The superior CO<sub>2</sub> electroreduction performance is attributed to the enhanced adsorption of key intermediate COOH\* on electron-rich Ni single atom, together with the dense active sites.

Electrochemical CO<sub>2</sub> reduction reaction (CO<sub>2</sub>RR) emerges as a carbon-neutral approach to recycle CO<sub>2</sub> and store intermittent renewable energies.<sup>[1]</sup> However, the chemical inertness of CO<sub>2</sub> molecule and its multiple reaction pathways with up to 16 possible products render electrocatalytic conversion processes energy-inefficient.<sup>[2]</sup> To achieve scalability for the technology, the reaction must occur at industrial-level currents at low overpotentials for ideally a single product. Currently, electrolyzers for CO<sub>2</sub> conversion to CO are reaching the pilot scale,<sup>[3]</sup> of which Au and Ag are the most promising catalysts.<sup>[4]</sup> Based on the membrane electrode assembly (MEA) device, the Au/InO<sub>2</sub> full cell feed with pure water achieved a CO current density of 300 mA cm<sup>-2</sup> at a cell voltage of ~2.65 V.<sup>[5]</sup> According to the industrial benchmarks for CO<sub>2</sub>-to-CO electrolysis proposed in 2021, there remains a big gap to achieve higher current densities (> 400 mA cm<sup>-2</sup>) at the lower cell voltages (< 2.5 V), by using non-precious metal catalysts.<sup>[3a]</sup>

Single-atom catalysts (SACs) with metal-N-C (Fe, Co, Ni, etc.) structures have demonstrated promising performance for CO<sub>2</sub> conversion.<sup>[6]</sup> Gu et al. have developed an atomically dispersed Fe<sup>3+</sup>-N-C that can deliver a CO partial current density of 94 mA cm<sup>-2</sup> at an overpotential of 340 mV.<sup>[7]</sup> Certain self-supported Ni-N-C membrane catalysts can produce CO with a high current density of 308.4 mA cm<sup>-2</sup> and 88% Faradaic efficiency (FE) in a flow cell.<sup>[8]</sup> Despite these breakthroughs, their single-atom nature with homogeneously dispersed active sites are only efficient in catalyzing single-molecule conversions.<sup>[9]</sup> For complex reactions that involve multiple intermediates, they generally show either too strong or too weak binding to one or more intermediates due to the scaling relationship.<sup>[10]</sup> For example, Ni-N-C sites typically exhibit very weak binding to COOH\* while Fe-N-C sites exhibit too strong binding to CO\*, both of which hinder efficient CO production.<sup>[11]</sup> Besides, the very low metal loading of SACs also severely limits their activity for practical applications.

Here, we show a cooperative Ni single-atom-on-nanoparticle catalyst (NiSA/NP) for energy-efficient CO<sub>2</sub> electroreduction. The design of this hybrid SAC enables: (i) electron density regulation of surface Ni-N-C by the encapsulated Ni nanoparticles for faster intermediate adsorption and desorption; (ii) *in situ* growth of high loading Ni single atoms on carbon nanotubes (CNTs) fed by Ni nanoparticles; (iii) a simple and scalable method for the mass synthesis of Ni SACs. The NiSA/NP catalyst achieves state-of-the-art CO<sub>2</sub>-to-CO performance in both the H-cell and zero-gap MEA full cells.

We pursued the nanoparticle co-catalysis effect by one-step solid-state pyrolysis with excessive Ni sources. The schematic diagram of the catalyst design and formation mechanism is shown in Fig. S1a. First, the melamine was decomposed into carbon nitride at ~400 °C.<sup>[12]</sup> With the increase of annealing temperature, the Ni nanoparticles catalyzed the carbon nitride to generate the carbon nanotubes (CNTs),<sup>[13]</sup> meanwhile Ni single atoms were trapped by the nitrogen-doped CNTs via thermal emitting.<sup>[14]</sup> The NiSA/NP was obtained after the heat treatment followed by the acid washing to remove the Ni nanoparticles outside of CNTs. Figure 1a shows the morphology of the NiSA/NP catalyst, where large amounts of Ni nanoparticles are confined inside of the nitrogen-doped CNTs. The EDS mapping confirms the presence of Ni and N in the carbon matrix, and evenly distributed Ni nanoparticles at micron-scale (Fig. S1d). The bright dots displayed in Fig. 1b are assigned to the Ni single atoms anchored on CNTs. For comparison, NiSA was prepared by the treatment of NiSA/NP with NH<sub>4</sub>Cl to remove Ni nanoparticles inside of the CNTs,<sup>[15]</sup> and NiNP was prepared by the nitrogen-free precursors (details in Methods section). As confirmed by TEM (Fig. 1c and Fig. S2) and X-ray diffraction (XRD, Fig. 1d), most of the Ni nanoparticles inside of CNTs were removed after the NH<sub>4</sub>Cl treatment while Ni single atoms remained. XRD also shows a dominant Ni(111) peak of the catalysts which is consistent with the DFT modelling. The XPS N 1s spectra of NiSA and NiSA/NP exhibit similar pyridinic (398.5

Dr. Wenhao Ren, Chen Jia, Qian Sun, Prof. Chuan Zhao  
School of Chemistry, University of New South Wales, Sydney, New South Wales 2052, Australia  
E-mail: chuan.zhao@unsw.edu.au  
Dr. Wenhao Ren, Prof. Xile Hu  
Laboratory of Inorganic Synthesis and Catalysis, Institute of Chemical Sciences and Engineering, Ecole Polytechnique Fédérale de Lausanne (EPFL), ISIC-LSCI, 1015 Lausanne  
E-mail: xile.hu@epfl.ch  
Dr. Xin Tan, Prof. Sean C. Smith  
Department of Applied Mathematics, Research School of Physics and Engineering, The Australian National University, Canberra, ACT 2601, Australia  
Anna Krammer, Dr. Andreas Schueler  
Solar Energy and Building Physics Laboratory, Ecole Polytechnique Fédérale de Lausanne, EPFL LESO-PB, 1015 Lausanne  
Dr. Jiangtao Qu  
Australian Centre for Microscopy and Microanalysis, University of Sydney, 2006, NSW, Australia.

Supporting information for this article is given via a link at the end of the document.

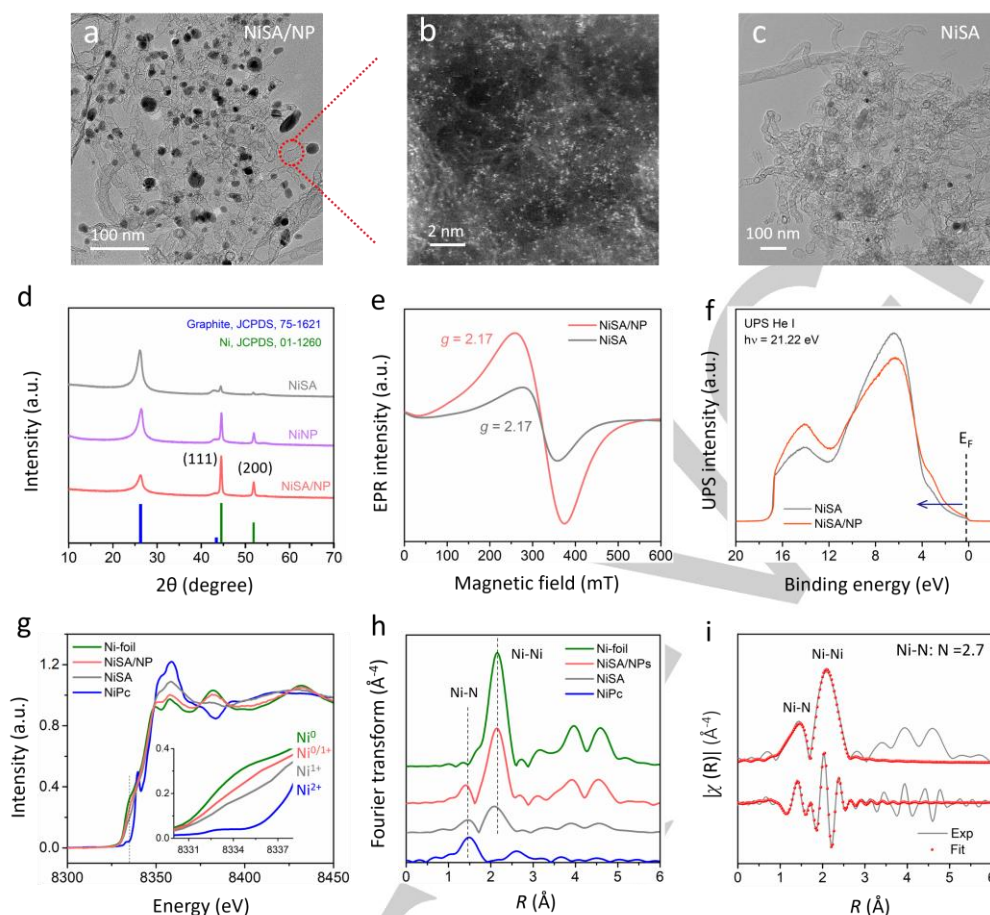


**Figure 1.** (a) Transmission electron microscopy (TEM) image of NiSA/NP. (b) High-angle annular dark-field scanning transmission electron microscopy (HAADF-STEM) image of NiSA/NP. (c) TEM image of NiSA. (d) X-ray diffraction results. (e) Electron paramagnetic resonance (EPR) spectra measured at 292 K. (f) UPS He I spectra of NiSA/NP and NiSA. (g) Ni K-edge XANES spectra of NiSA/NP and NiSA with the comparison of standard NiPc and Ni foil. The inset shows the enlarged pre-edge region. (h) The plotted Fourier transformation of extended X-ray absorption fine structure (FT-EXAFS) spectra of NiSA/NP, NiSA, Ni-foil, and NiPc. (i) EXAFS fitting of NiSA.

eV), pyrrolic (401.2 eV), graphitic (402.7 eV), and Ni-N (399.4 eV) peaks (Fig. S4b,c), indicative of the identical Ni-N-C structure after the removal of Ni nanoparticles. According to the ICP-OES (Table S1), the Ni contents in NiSA/NP and NiSA are 8.8 wt% and 4.6 wt%, respectively. The high content of Ni single atom can be attributed to (i) the *in-situ* formation of Ni-N-C during the growth of CNTs and (ii) the excessive Ni sources provided by the Ni nanoparticles.

The unpaired electron in catalysts was directly observed by EPR spectroscopy (Fig. 1e), where a  $g$ -value of 2.17 is obtained for both samples and could be assigned to the unpaired electron in the  $3d_{x^2-y^2}$  orbital of Ni(i).<sup>[16]</sup> The EPR signal intensity of NiSA/NP is above 2 times higher than NiSA, corresponding to the electron-rich structure due to the presence of Ni nanoparticles. We further examined the d band structure of Ni using ultraviolet photoelectron spectroscopy (UPS, Fig. 1f and Fig. S5). No obvious metallic Ni peak can be observed across the Fermi level, which can be attributed to the fully confined Ni nanoparticles inside of CNTs that exceeded the detection limit of UPS (2-3 nm), in line with XPS results (Fig. S4a). Therefore, the shift of near Fermi level signals (0-1 eV) can be attributed to the

change of electronic structure of Ni single atoms on the surface of CNTs. The position of NiSA increases in binding energy compared to NiSA/NP (away from the Fermi level). According to d band theory, the downshifted d band of NiSA (grey curve) corresponds to a weakened adsorption strength.<sup>[17]</sup>

The Ni K-edge X-ray absorption near-edge structure (XANES) and extended X-ray absorption fine structure (EXAFS) measurements were carried out to identify the electronic structure and coordination environment of catalysts. Ni foil and NiPc were used as references for metallic Ni and Ni<sup>2+</sup>, respectively. The pre-edge curve of NiSA is in the middle of Ni foil and NiPc (Fig. 1g), suggesting a valence state of Ni close to +1.<sup>[18]</sup> Ni(i)-N-C has been revealed as a highly active site for CO<sub>2</sub>-to-CO conversion.<sup>[16a]</sup> More importantly, the pre-edge position of NiSA/NP is between the Ni foil and NiSA, corresponding to an even lower average valence state than Ni<sup>+</sup>. The Fourier-transformed  $k^3$ -weighted spectra of the samples exhibit two major peaks at 1.45 Å and 2.1 Å, which are assigned to Ni-N and Ni-Ni coordination shells, respectively (Fig. 1h). The significantly decreased Ni-Ni peak intensity in NiSA compared with NiSA/NP corresponds to the removal of Ni nanoparticles.

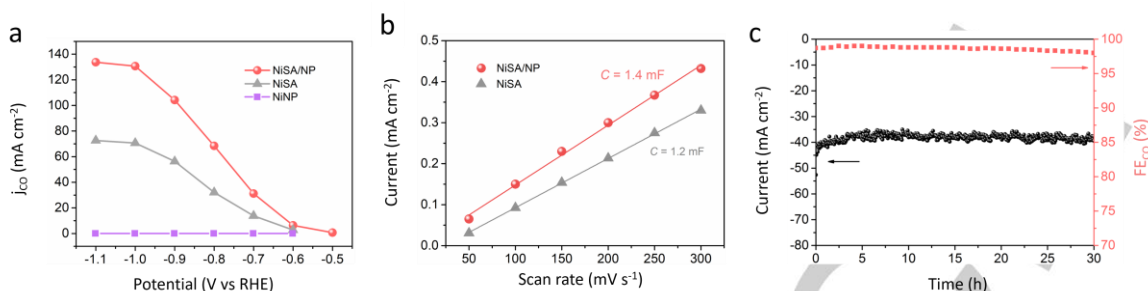


**Figure 2.** CO<sub>2</sub>RR in H-cells. (a) Partial CO currents plotted against different potentials. (b) Double-layer capacitance of two different electrodes. (c) Stability testing of NiSA/NP at -0.75 V vs. RHE for 30 h electrolysis.

Note that the Ni-Ni peak can be easily observed even there are only residual Ni NPs in the catalysts.<sup>[19]</sup> Based on the EXAFS fitting of Ni-N shell on NiSA, the average coordination number is determined to be 2.7. Given the high temperature (1000 °C) pyrolysis is used for the synthesis of catalysts, the Ni-single-sites should be thermodynamically uniform and thus we assign the structure of single atom to NiN<sub>3</sub> (Fig. 1i and Table S3),<sup>[20]</sup> although some NiN<sub>2</sub> or NiN<sub>4</sub> could exist.

The electrochemical testing was firstly conducted in an H-cell using 0.5 M KHCO<sub>3</sub> electrolyte and the corresponding calibration curve is shown in Fig. S6. Figure 2a displays the partial CO currents at different potentials, where the NiSA/NP outperforms the NiSA in a wide potential window, achieving a high current density of 131 mA cm<sup>-2</sup> at -1.0 V vs RHE which is almost doubled compared to NiSA. To the best of our knowledge, this result outperforms most, if not all, CO<sub>2</sub>-to-CO catalysts in H-cells reported to date (Table S4). The Faradic efficiency of CO (FE<sub>CO</sub>) is shown in Fig. S7b, where NiSA/NP can achieve an ultra-high FE<sub>CO</sub> above 99% at -0.8 V. In comparison, pure NiNP without Ni-N-C can only catalyze the HER without any CO<sub>2</sub>RR products detected (Fig. S7). The pure NiSA without nanoparticles was further prepared via multi-step NH<sub>4</sub>Cl treatment (Fig. S8). The FE<sub>CO</sub> and *j*<sub>CO</sub> of NiSA-3 were further decreased after completely removing the Ni nanoparticles inside of CNTs. The electrochemically active surface area (ECSA) is evaluated from double-layer capacitance (*C*<sub>dl</sub>) to elucidate the origin of the enhanced catalytic activity on NiSA/NP.<sup>[21]</sup> The NiSA/NP shows slightly higher *C*<sub>dl</sub> compared with NiSA (1.4 mF vs 1.2 mF), suggesting that the improved catalytic activity is primarily attributed to the intrinsic reactivity of each site, rather than a surface area effect (Fig. 2b). Stability testing is then performed at -0.75 V vs RHE, NiSA/NP shows robust durability for CO<sub>2</sub>RR during 30 hours of continuous electrolysis, maintaining constant current densities and 99% of the initial FE for CO production (Fig. 2c).

To assess the performance of catalysts at industrial-relevant devices and current densities, we further evaluate the CO<sub>2</sub>RR in flow cells using gas diffusion electrodes (Fig. S9). Figure 3a displays the CO FEs and partial current densities plotted against the *iR*-corrected potentials in 1 M KOH flow cells. The NiSA/NP shows a low onsite potential at around -0.25 V vs RHE. Then, the CO partial currents quickly increase to above 200 mA cm<sup>-2</sup> at -0.4 V with FE<sub>CO</sub> of 96%, and further reach 346 mA cm<sup>-2</sup> at -0.5 V with FE<sub>CO</sub> of 98%. As a comparison, the highest current obtained with NiSA is 263 mA cm<sup>-2</sup> at -0.65 V (Fig. S10). The

superior CO<sub>2</sub>RR performance of NiSA/NP in the flow cell can be attributed to (i) the significantly enhanced CO<sub>2</sub> mass transport based on gas diffusion electrode and (ii) the catalytic promotion effect in alkaline electrolytes.<sup>[22]</sup> To evaluate the stability of NiSA/NP from a device point of view, galvanostatic measurement at 100 mA cm<sup>-2</sup> was performed based on the flow cell. NiSA/NP shows moderate durability (Fig. 3b), starting at -0.31 V vs RHE and gradually increases to -0.37 V after 10 hours of electrolysis. On the other hand, the catalysts can maintain a very stable FE<sub>CO</sub> above 98% throughout the testing. Given that the overall structure of carbon and Ni are preserved after testing, we attributed the decay to the flooding of the GDE (Fig. S11).

The full cell performance was then tested based on the zero-gap MEA device, which is regarded as a promising prototype for practical application because of the very low cell resistance and robust structure. Fig. 3c exhibits the LSV curves of two different full cells by using IrO<sub>2</sub> and NiFe anodes, respectively. With 1 M KOH as the anolyte, the NiSA/NP||NiFe cell shows even better performance than the widely used IrO<sub>2</sub> anode. It is worth noting that the Ir-based anode can cost more than 60% of the total price of MEA device,<sup>[3a]</sup> so that the development of the low-cost substitution is highly desirable. As shown in Fig. 3d, the NiSA/NP||NiFe cell delivers a *j*<sub>CO</sub> of 163 mA cm<sup>-2</sup> with FE<sub>CO</sub> of 92% at -2.0 V without *iR* compensation. With further increase of cell voltage to -2.3 V, the *j*<sub>CO</sub> can reach up to 310 mA cm<sup>-2</sup> with

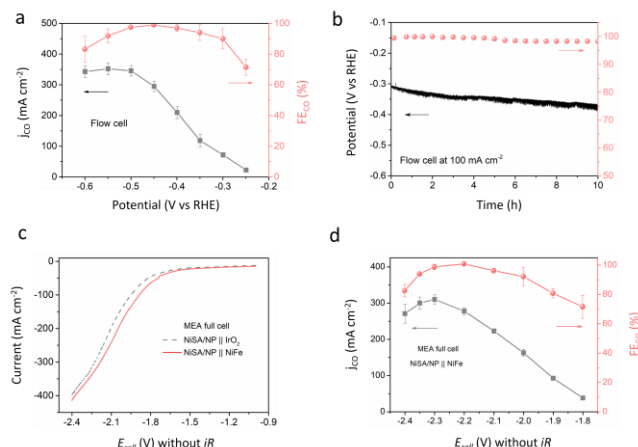


**Figure 3.** Gas diffusion electrode-based devices for CO<sub>2</sub>RR on NiSA/NP. (a) *j*<sub>CO</sub> and FE<sub>CO</sub> at different potentials in 1 M KOH flow cells. (b) Galvanostatic measurement at 100 mA cm<sup>-2</sup>. (c) Polarisation curves obtained at a scan rate of 10 mV s<sup>-1</sup> in the zero-gap MEA full cells with IrO<sub>2</sub> and NiFe as the anodes, and 1 M KOH as the anolyte. (d) *j*<sub>CO</sub> and FE<sub>CO</sub> in the MEA full cell.

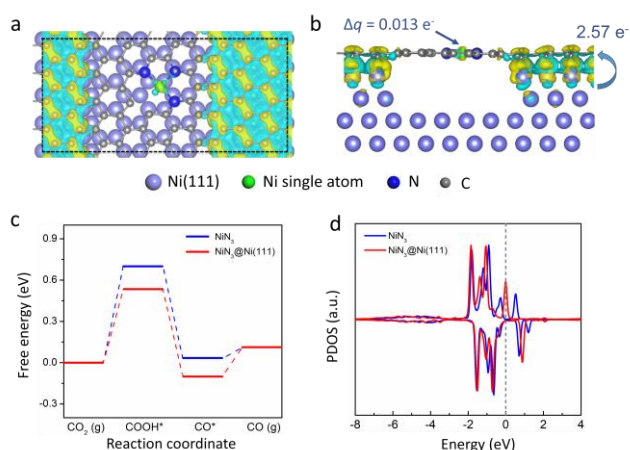


**Figure 4.** Density functional theory (DFT) calculations. (a,b) Top and side views of the deformation electronic densities of NiN<sub>3</sub>@Ni(111).  $\Delta q$  indicates the increased number of electrons of the Ni single atom on NiN<sub>3</sub>@Ni(111). (c) The calculated free energy diagrams for CO<sub>2</sub>RR to CO on NiN<sub>3</sub> and NiN<sub>3</sub>@Ni(111). (d) The projected density of states (PDOS) of d orbitals of Ni atoms on NiN<sub>3</sub>@Ni(111) and NiN<sub>3</sub>. The dotted grey lines indicate the Fermi level.

FE<sub>CO</sub> of ~99%, corresponding to an outstanding full cell energy efficiency of 57%. Note that certain Ag-based MEA devices can achieve current densities above 600 mA cm<sup>-2</sup> but at a much higher cell voltage of -3.5 V with a low energy efficiency of ~35%.<sup>[23]</sup> To our knowledge, the NiSA/NPIINiFe cell shows the state-of-the-art energy efficiency for CO production at an industrially relevant current density of ~300 mA cm<sup>-2</sup> (Table S5).

DFT calculations were then performed via deformation electronic density calculation and Bader analysis. Here NiN<sub>3</sub> site combined with face-centered cubic Ni(111) is used as the targeted structure according to the XAS and XRD results (Fig. 1d,i). Given that most NiN<sub>3</sub> sites are surrounded by Ni nanoparticles rather than direct contact (Fig. 1a), the DFT model was established as shown in Figure 4a,b. The results indicate that the first layer of Ni(111) can easily bind with the adjacent carbon, which leads to a significant electron transfer from Ni(111) to NiN<sub>3</sub> layer (2.57 e<sup>-</sup>). Bader analysis shows that more electrons are accumulated on the Ni single atom in the presence of Ni(111) ( $\Delta q = 0.013$  e<sup>-</sup>).

We next shift our attention to study the CO<sub>2</sub>RR activities of NiN<sub>3</sub>@Ni(111) and NiN<sub>3</sub>. Here, COOH\* and CO\* are considered as intermediates for electrochemical CO<sub>2</sub>-to-CO conversion.<sup>[24]</sup> As shown in Figure 4c, the rate-limiting step on bare NiN<sub>3</sub> is CO<sub>2</sub>(g)→COOH\* with a free energy of 0.70 eV because of the weak binding of COOH\* on NiN<sub>3</sub>, consistent with previous reports.<sup>[1b]</sup> After incorporating Ni(111) into the structure, the binding strength of COOH\* on NiN<sub>3</sub> is greatly enhanced and the  $\Delta G$  decreases by 0.17 eV. In comparison with the neutral cases, the stronger binding of COOH\* on negatively charged NiN<sub>3</sub> reduces the overpotential of CO<sub>2</sub>RR and enhances their activities. In addition, we calculated the projected density of states (PDOS) of Ni d orbitals of NiN<sub>3</sub> moiety with and without Ni(111) (Fig. 4d). An obvious right shift of PDOS of Ni d orbitals is observed on NiN<sub>3</sub>@Ni(111) compared to bare NiN<sub>3</sub>, which results in stronger binding of intermediates.

Note that the electrons on NiN<sub>3</sub> sites could vary depending on the density of Ni nanoparticles around it. In this case, we

introduce a second DFT model based on Ni(111)/carbon and manually inject different electrons to NiN<sub>3</sub> structure to investigate the change of intermediates adsorption (Fig. S14). Similar to the NiN<sub>3</sub>@Ni(111) model (Fig. 4c), the free energy of COOH\* decreases as the increase of the electrons injected to the structure, which is beneficial to the CO<sub>2</sub>RR.

In conclusion, a cooperative Ni SAC via nanoparticles coupling was firstly synthesized by a direct solid-state pyrolysis. Extensive structural characterizations revealed a low valence of Ni single atom with abundant unpaired d-electrons in the structure. DFT simulations showed electron enrichment of single-Ni-sites with enhanced binding to the key intermediate COOH\*. Thus, the greatly enhanced CO<sub>2</sub>RR activity on NiSA/NP is understood as a result of its tuned electronic configuration. Together with the populated Ni single atom (4.6 wt%), a state-of-the-art performance is achieved in the MEA full cell, which delivered a high CO current density of 310 mA cm<sup>-2</sup> at -2.3 V with an overall energy efficiency of 57%. This work opens a new avenue for the design of cooperative SACs, which can potentially be used for a range of technologically important catalytic reactions.

## Acknowledgements

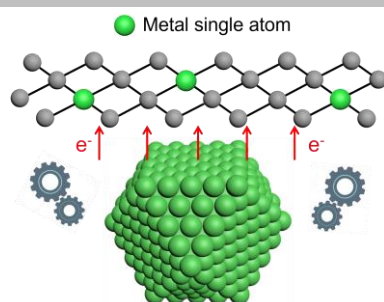
W.R. and X.T. contributed equally to this work. This work was supported by the Australian Research Council (FT170100224, DP210103892). The authors are thankful to Dr. Jun Gu for his help in the assembly of flow cell and membrane electrolyser, and Australia Synchrotron center (ANSTO), and UNSW Mark Wainwright Analytical Center for providing access to their XAFS, XRD, SEM, XPS, NMR and facilities. This research was also undertaken with the assistance of resources provided by the National Computing Infrastructure (NCI) facility at the Australian National University; allocated through both the National Computational Merit Allocation Scheme supported by the Australian Government and the Australian Research Council grant LE190100021 (Sustaining and strengthening merit-based access at NCI, 2019-2021). This project has received funding from the European Union's Horizon 2020 research and innovation programme under the Marie Skłodowska-Curie grant agreement (891545-ADBCRZB). The work is part of NCCR Catalysis, a National Centre of Competence in Research funded by the Swiss National Science Foundation.

**Keywords:** Cooperative single-atom catalyst • electronic regulation • metal-nitrogen-carbon • electrocatalyst • CO<sub>2</sub> reduction

- [1] a) M. B. Ross, P. De Luna, Y. Li, C.-T. Dinh, D. Kim, P. Yang, E. H. Sargent, *Nat. Catal.* **2019**, *2*, 648-659; b) W. Ju, A. Bagger, G. P. Hao, A. S. Varela, I. Sinev, V. Bon, B. Roldan Cuenya, S. Kaskel, J. Rossmeisl, P. Strasser, *Nat. Commun.* **2017**, *8*, 944; c) M. G. Kibria, J. P. Edwards, C. M. Gabardo, C. T. Dinh, A. Seifitokaldani, D. Sinton, E. H. Sargent, *Adv. Mater.* **2019**, 1807166; d) C. S. Diercks, Y. Liu, K. E. Cordova, O. M. Yaghi, *Nat. Mater.* **2018**, *17*, 301.

- [2] a) S. Chu, Y. Cui, N. Liu, *Nat. Mater.* **2017**, *16*, 16; b) M. Zhong, K. Tran, Y. Min, C. Wang, Z. Wang, C.-T. Dinh, P. De Luna, Z. Yu, A. S. Rasouli, P. Brodersen, *Nature* **2020**, *581*, 178-183.
- [3] a) R. I. Masel, Z. Liu, H. Yang, J. J. Kaczur, D. Carrillo, S. Ren, D. Salvatore, C. P. Berlinguette, *Nat. Nanotechnol.* **2021**, *16*, 118-128; b) R. Krause, D. Reinisch, C. Reller, H. Eckert, D. Hartmann, D. Taroata, K. Wiesner-Fleischer, A. Bulan, A. Lueken, G. Schmid, *Chem. Ing. Tech.* **2020**, *92*, 53-61.
- [4] S. Zhao, R. Jin, R. Jin, *ACS Energy Lett.* **2018**, *3*, 452-462.
- [5] Z. Yin, H. Peng, X. Wei, H. Zhou, J. Gong, M. Huai, L. Xiao, G. Wang, J. Lu, L. Zhuang, *Energy Environ. Sci.* **2019**, *12*, 2455-2462.
- [6] M. Li, H. Wang, W. Luo, P. C. Sherrell, J. Chen, J. Yang, *Adv. Mater.* **2020**, *32*, 2001848.
- [7] J. Gu, C.-S. Hsu, L. Bai, H. M. Chen, X. Hu, *Science* **2019**, *364*, 1091-1094.
- [8] H. Yang, Q. Lin, C. Zhang, X. Yu, Z. Cheng, G. Li, Q. Hu, X. Ren, Q. Zhang, J. Liu, *Nat. Commun.* **2020**, *11*, 1-8.
- [9] J. Jiao, R. Lin, S. Liu, W.-C. Cheong, C. Zhang, Z. Chen, Y. Pan, J. Tang, K. Wu, S.-F. Hung, *Nat. Chem.* **2019**, *11*, 222-228.
- [10] J. Pérez-Ramírez, N. López, *Nat. Catal.* **2019**, *2*, 971-976.
- [11] W. Ren, X. Tan, W. Yang, C. Jia, S. Xu, K. Wang, S. C. Smith, C. Zhao, *Angew. Chem. Int. Ed.* **2019**, *58*, 6972-6976.
- [12] R. C. Dante, P. Martín-Ramos, A. Correa-Guimaraes, J. Martín-Gil, *Mater. Chem. Phys.* **2011**, *130*, 1094-1102.
- [13] J. Meng, C. Niu, L. Xu, J. Li, X. Liu, X. Wang, Y. Wu, X. Xu, W. Chen, Q. Li, *J. Am. Chem. Soc.* **2017**, *139*, 8212-8221.
- [14] a) C. Zhao, Y. Wang, Z. Li, W. Chen, Q. Xu, D. He, D. Xi, Q. Zhang, T. Yuan, Y. Qu, *Joule* **2019**, *3*, 584-594; b) Y. Qu, Z. Li, W. Chen, Y. Lin, T. Yuan, Z. Yang, C. Zhao, J. Wang, C. Zhao, X. Wang, *Nat. Catal.* **2018**, *1*, 781-786.
- [15] M. X. Chen, M. Zhu, M. Zuo, S. Q. Chu, J. Zhang, Y. Wu, H. W. Liang, X. Feng, *Angew. Chem. Int. Ed.* **2020**, *59*, 1627-1633.
- [16] a) H. B. Yang, S.-F. Hung, S. Liu, K. Yuan, S. Miao, L. Zhang, X. Huang, H.-Y. Wang, W. Cai, R. Chen, *Nat. Energy* **2018**, *3*, 140; b) T. Wongnate, D. Sliwa, B. Ginovska, D. Smith, M. W. Wolf, N. Lehnert, S. Raugel, S. W. Ragsdale, *Science* **2016**, *352*, 953-958.
- [17] B. Hammer, J. K. Nørskov, *Adv. Catal.* **2000**, *45*, 71-129.
- [18] T. Zhang, X. Han, H. Yang, A. Han, E. Hu, Y. Li, X. q. Yang, L. Wang, J. Liu, B. Liu, *Angew. Chem.* **2020**, *132*, 12153-12159.
- [19] L. Cao, Q. Luo, W. Liu, Y. Lin, X. Liu, Y. Cao, W. Zhang, Y. Wu, J. Yang, T. Yao, S. Wei, *Nat. Catal.* **2018**.
- [20] X. Wang, Z. Chen, X. Zhao, T. Yao, W. Chen, R. You, C. Zhao, G. Wu, J. Wang, W. Huang, J. Yang, X. Hong, S. Wei, Y. Wu, Y. Li, *Angew. Chem.* **2018**, *57*, 1944-1948.
- [21] D. Voiry, M. Chhowalla, Y. Gogotsi, N. A. Kotov, Y. Li, R. M. Penner, R. E. Schaak, P. S. Weiss, *ACS Nano* **2018**, *12*, 9635-9638.
- [22] C.-T. Dinh, T. Burdyny, M. G. Kibria, A. Seifitokaldani, C. M. Gabardo, F. P. G. de Arquer, A. Kiani, J. P. Edwards, P. De Luna, O. S. Bushuyev, *Science* **2018**, *360*, 783-787.
- [23] B. Endródi, A. Samu, E. Kecsenovity, T. Halmágyi, D. Sebők, C. Janáky, *Nat. Energy* **2021**, *6*, 439-448.
- [24] R. Kortlever, J. Shen, K. J. P. Schouten, F. Calle-Vallejo, M. T. Koper, *J. Phys. Chem. Lett.* **2015**, *6*, 4073-4082.

**Cooperative Ni single-atom on nanoparticle catalyst** is developed. With the electron donation from Ni nanoparticle to the single atom via the carbon network, the catalysts achieve high CO current density of 310 mA cm<sup>-2</sup> at -2.3 V with an overall energy efficiency of 57% for electrochemical CO<sub>2</sub> reduction.



Wenhao Ren,<sup>†</sup> Xin Tan,<sup>†</sup> Chen Jia,  
Anna Krammer, Qian Sun, Jiangtao Qu,  
Sean C. Smith, Andreas Schueler, Xile  
Hu\* and Chuan Zhao\*

Page No. – Page No.

**Electronic regulation of Ni single  
atom by confined Ni nanoparticles for  
energy-efficient CO<sub>2</sub> electroreduction**